Optimizing Volumetric Efficiency and Backscatter Communication in Biosensing Ultrasonic Implants

Mohammad Meraj Ghanbari ⓘ, *Student Member, IEEE*, and Rikky Muller, *Senior Member, IEEE*

Abstract—Ultrasonic backscatter communication has gained popularity in recent years with the advent of deep-tissue sub-mm scale biosensing implants in which piezoceramic (piezo) resonators are used as acoustic antennas. Miniaturization is a key design goal for such implants to reduce tissue displacement and enable minimally invasive implantation techniques. Here, we provide a systematic design approach for the implant piezo geometry and operation frequency to minimize the overall volume of the implant. Optimal geometry of the implant piezo for backscatter communication is discussed and contrasted with that of power harvesting. A critical design aspect of an ultrasonic backscatter communication link is the response of the piezo acoustic reflection coefficient Γ with respect to the variable shunt impedance, Z_E, of the implant uplink modulator. Due to the complexity of the piezo governing equations and multi-domain, electro-acoustical nature of the piezo, $\Gamma(Z_E)$ has often been characterized numerically and the implant uplink modulator has been designed empirically resulting in sub-optimal performance in terms of data rate and linearity. Here, we present a SPICE friendly end-to-end equivalent circuit model of the channel as a piezo-IC co-simulation tool that incorporates inherent path losses present in a typical ultrasonic backscatter channel. To provide further insight into the channel response, we present experimentally validated closed form expressions for $\Gamma(Z_E)$ under various boundary conditions. These expressions couple Γ to the commonly used Thevenin equivalent circuit model of the piezo, facilitating systematic design and synthesis of ultrasonic backscatter uplink modulators.

Index Terms—Backscatter, circuit model, echo modulation, implant, modulator, piezoelectric, ultrasound, wireless.

I. INTRODUCTION

A GROWING number of ultrasonic mm-scale implants have recently been proposed for interacting with deeply-seated human nerves [1]–[4] and monitoring a wide range of physiological signals, such as pressure [5], temperature [6], [7], blood oxygen saturation [8], gastric waves [9] and tissue impedance [10] from deep anatomical regions. Reported implant volumes
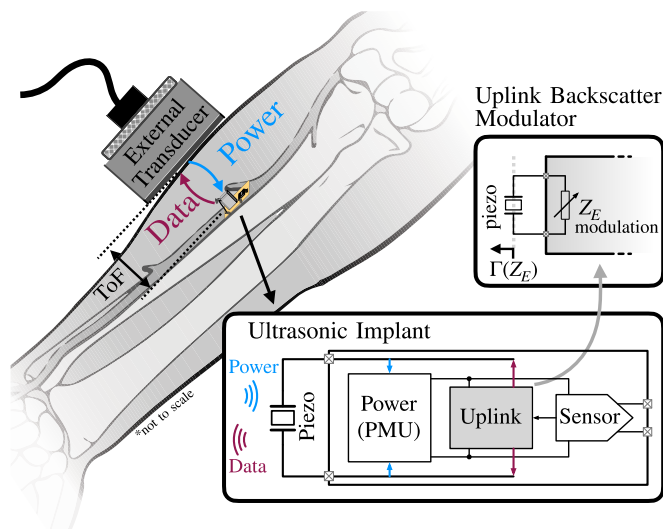

Fig. 1. Single-piezo ultrasonic biosensing implant with backscatter uplink modulator.

as small as 0.065 mm^3 [7], *in vitro* wireless operation ranges of up to 12 mm [5] and fully untethered *in vivo* implantation in live rodents [3] demonstrate the potential of miniaturized ultrasonically powered implants as a viable solution for deep-tissue therapy and biosensing.

The basic components of an ultrasonic implant, conceptually shown in Fig. 1, are a piezoceramic resonator (or piezo) and an integrated circuit (IC). The implant piezo functions as an acoustic antenna enabling the implant to harvest energy from ultrasound waves launched by a distant external transducer (interrogator). The power management unit (PMU) of the implant IC conditions the harvested energy for signal acquisition and data back telemetry. The acquired signal is wirelessly transmitted to the external transducer by the uplink modulator of the IC. For implantable devices, to reduce tissue displacement and enable minimally invasive non-surgical implantation techniques, *e.g.* injection, the overall implant volume should be kept small, *e.g.* sub-mm^3. Given that the volume of the implant is dominated by the piezo, the majority of the aforementioned prior art use a single-piezo implant assembly where data uplink is realized by modulating the amplitude of the ultrasound echo reflected from the implant piezo (backscattering). For ultra-low power biosensing ICs, backscatter communication obviates the need for external capacitors or a secondary piezo and consequently results in the smallest possible implant form factor [2], [7].

The focus of this work is twofold. Using the concept of piezo volumetric efficiency, we first present a systematic design approach to minimize the overall volume of the implant provided the power consumption and the equivalent input resistance of the IC are known. We then perform a thorough characterization of the ultrasonic backscatter communication channel to help advance state-of-the-art uplink backscatter modulators in terms of data rate and linearity. The uplink backscatter modulator in Fig. 1 in its simplest representation is a variable shunt impedance Z_E connected across the piezo terminals that modulates the acoustic reflection coefficient of the piezo Γ. Resistive [11], capacitive [12] and FET [1], [7] shunt modulating networks have been previously explored. Due to lack of a tool for piezo-IC co-simulation or any known analytical relationship between Γ and the uplink modulating impedance Z_E, previous implementations of digital backscatter modulators have been limited to the most basic type of digital modulation (on-off keying, OOK) [7], [8], and previously reported analog backscatter modulators have been designed empirically and suffered from significant nonlinearity [1], [6]. We therefore pay special attention to the characterization of $\Gamma(Z_E)$ and provide an end-to-end equivalent circuit model of the channel for piezo-IC co-simulation in a common CAD tool. Moreover, we further expand the analysis presented recently in [13] and provide universal closed-form expressions for $\Gamma(Z_E)$ to include: 1) Γ's dependence on Z_E at both the series and parallel resonant frequencies 2) the effect of low-Q mechanically damped piezo, and 3) the effect of air-backing. We briefly discuss how one can leverage the derived analytical closed form expressions to improve the linearity of an analog backscatter modulator or implement amplitude shift keying digital modulation to enhance the data rate of a digital backscatter modulator relative to the commonly used OOK modulation. The derived expressions require only a single parameter, piezo internal impedance, that can easily be measured or accurately simulated prior to any piezo-circuit codesign. The results (Γ vs. Z_E) predicted by the derived expressions are shown to be in good agreement with those obtained by the finite element method (FEM) simulation and experiments, validating their accuracy.

The manuscript is organized as follows: optimal geometrical design of the implant piezo is discussed in Section II from power harvesting perspectives. In Section III, an overview of the backscatter protocol is presented, and various channel path loss components are discussed and evaluated. An end-to-end SPICE friendly equivalent circuit model of the channel used to numerically solve for $\Gamma(Z_E)$ is presented in Section IV. Closed-form expressions for $\Gamma(Z_E)$ under various boundary conditions are introduced in Section V. Section VI discusses optimal geometrical design of the impant piezo for backscatter communication. Experimental verification of the derived expressions is presented in Section VII, and Section VIII concludes the paper.

II. IMPLANT PIEZO MINIATURIZATION

The geometry of the implant piezo is a critical design parameter since it determines the volume of the implant, the operating frequency, and the harvested power made available to the implant IC. Design variables are the thickness (T) and aspect ratio (AR) of the piezo. We define AR as the ratio of the piezo width

to its thickness as illustrated in Fig. 2(a). In this section, we discuss different characteristics of the implant piezo from power harvesting and delivery perspectives and provide a systematic design approach for the implant piezo geometry and operation frequency with the objective of piezo miniaturization.

Mechanical resonant modes of bulk piezos with moderate aspect ratios suitable for implants can be classified to width expander (WE) and longitudinal expander (LE) for respectively large (>1) and small (<1) aspect ratios (ARs). In each mode, the piezo mechanically resonates along its major dimension, width or thickness respectively. Although, piezoelectric constitutive equations exist for the two resonant modes that can be used for analysis [14], for this study, we used a parametric FEM simulation (using COMSOL Multiphysics) because the two resonant modes are strongly coupled for AR ~ 1 and are not well-described by a single set of equations. We used a 2D axisymmetric model of the piezo with a surface area equivalent to that of a cuboid shown in Fig. 2(a). A common piezo material (lead zirconated titanite, PZT-5H, with a mechanical quality factor of 50 and a dielectric loss tangent of 0.02) was used, while the model included a tissue phantom with the specific acoustic impedance of 1.5 MRayls surrounding the implant piezo. The model was encapsulated with a perfectly matched layer, while frequency domain analyses were used for simulating the impedance and harvested power.

The link operating frequency is often chosen to be the resonant frequency of the implant piezo because: (1) at resonance the piezo has the highest electromechanical transduction efficiency and exhibits a resistive internal impedance. Therefore, maximum power delivery to the IC can be obtained without impedance matching networks; (2) more importantly, as demonstrated in Section VII, the implant uplink modulator has the maximum backscatter modulation strength at the piezo resonant frequencies. Figs. 2(b) and (c) show the simulated series, f_s, and parallel resonant frequencies, f_p, of the piezo for thicknesses ranging from 100 μm to 1000 μm and aspect ratios ranging from $1/4$ to 4. AR$<1/4$ is impractical due to mechanical fragility and therefore ignored in this study.

At resonance, the piezo can be modeled by its Thevenin equivalent circuit, shown in Fig. 2(a). It can be shown that in general R_{Th} is a function of AR and V_{Th} is linearly proportional to the piezo thickness as simulated and shown in Figs. 2(d) and (e). The simulated V_{Th} in Fig. 2(e) was found by applying an incident (background) pressure field of $p_i = 147$ kPa (equivalent to the regulated pressure intensity of 720 mW/cm^2 in tissue [15]), and recording the open-circuit voltage of the implant piezo for all the geometries. The impedance of the piezo was simulated in absence of the background field using a test voltage source connected across the piezo terminals. The simulated V_{Th} and R_{Th} were used to calculate the available power, P_a, by the piezo for all the possible geometrical configurations (T and AR). Because the implant piezo is non-planar, volumetric efficiency (P_a per unit volume) is used as a figure of merit when comparing different configurations, as shown in Fig. 2(f).

The simulated volumetric efficiency shown in Fig. 2(f) is grouped based on the aspect ratio and the type of the resonant frequency. It is observed for a fixed AR, the piezo thickness can be used as a proxy to trade P_a with the volume of the
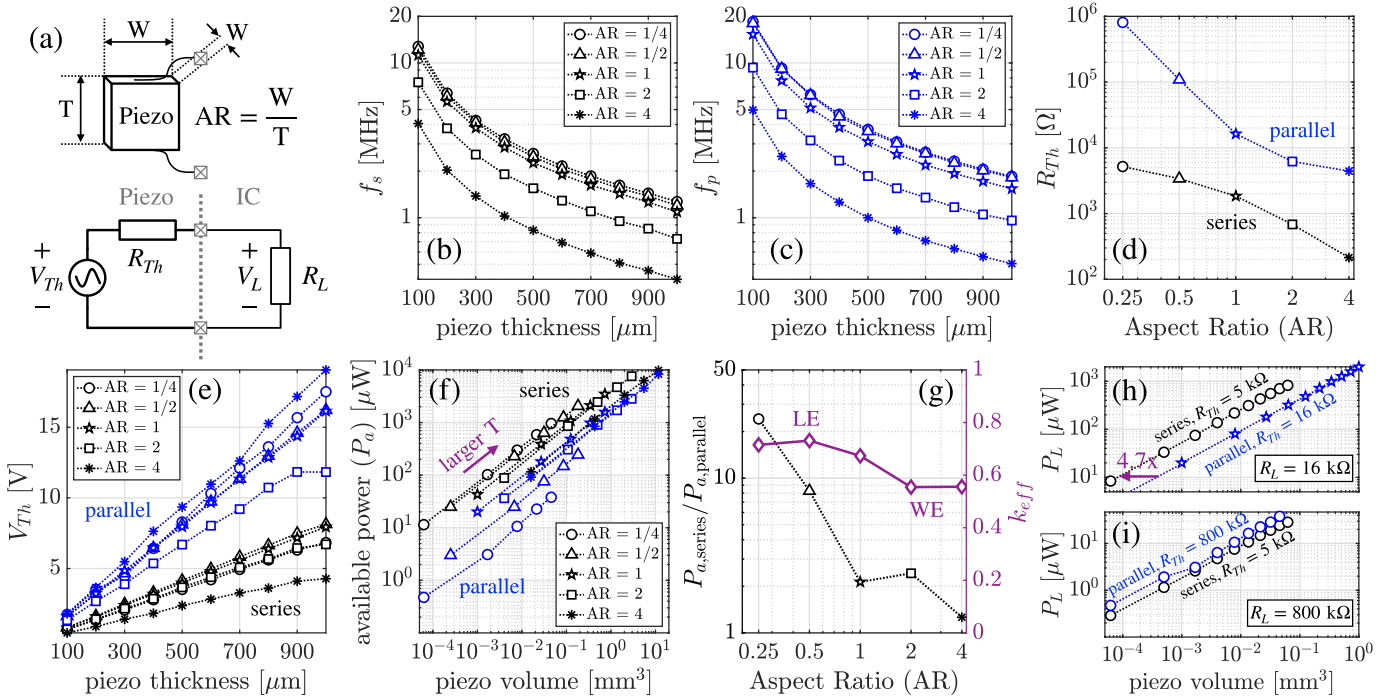
Fig. 2. (a) Implant piezo geometry and its Thevenin equivalent circuit at resonance. Finite Element Simulation (FEM) results of the (b) series resonant frequency, (c) parallel resonant frequency, (d) resistance and (e) open circuit voltage with an incident pressure intensity of 720 mW/cm^2 for various piezo thicknesses and aspect ratios. (f) Simulated V_{Th} and R_{Th} values in (d) and (e) were used to calculate the available power per unit volume of the implant piezo (volumetric efficiency) at f_s and f_p. (g) Relative available power at f_s and f_p and its correlation with piezo resonant modes: Longitudinal Expander (LE) and Width Expander (WE) resonant modes determined using the effective electromechanical coupling factor of the piezo, k_{eff}. (h) A design example when operating at f_s with a relatively small impedance mismatch results in a smaller piezo volume compared to operating at f_p with a perfect piezo-load impedance matching. (i) A design example when operating at f_s with a relatively large impedance mismatch results in a larger piezo volume compared to operating at f_p with a perfect piezo-load impedance matching. Note: In all plots, each aspect ratio is shown using a unique marker (e.g., $\triangle$ for AR = 1/2).

piezo. But because the slope of the curves in Fig. 2(f) is only 6.6 dB/decade, trading P_a with the piezo volume degrades the volumetric efficiency of the piezo. Instead of thickness, the aspect ratio of the piezo can be used to improve the volumetric efficiency. At f_s, decreasing the aspect ratio asymptotically improves the volumetric efficiency as shown in Fig. 2(f). A similar but opposite trend is found at f_p, that is increasing the AR enhances the volumetric efficiency.

The final parameter for improving the volumetric efficiency is the type of the resonant frequency. As shown in Fig. 2(f), a piezo operating at f_s generally provides a larger P_a per unit volume compared to f_p. This discrepancy in P_a is more evident for smaller aspect ratios as demonstrated in Fig. 2(g) and can be explained as follows. The piezo converts acoustical energy carried by pressure waves to electrical energy. The input acoustical energy to the piezo is maximum when the pressures exerted on the opposite sides of the piezo are in phase, i.e. out-of-phase pressures result in a net force acting on the piezo body without creating any internal stress/strain. The phase shift of the incident acoustic wave measured across the front and back faces of an implanted piezo in tissue is given by $\theta = 2\pi f T / v_{tissue}$, where f is the wave frequency and v_{tissue} is the propagation speed of sound in tissue (for most tissue types is ~ 1500 m/s [16]). Resonant frequencies of an LE-resonating piezo are $f_p = v_{piezo}/2T$ and $f_s = f_p \sqrt{1 - k_{eff}^2}$ [14], where v_{piezo} is the speed of sound in the piezo material (~ 4500 m/s for PZT-5H) and k_{eff} is the effective electromechanical coupling factor of the piezo that

is ~ 0.7 as shown in Fig. 2(g). Therefore, $\theta_{parallel} \sim 3\pi$, but $\theta_{series} \sim 2\pi$ for small ARs. That is, small aspect ratios increase k_{eff} and decrease θ_{series} ultimately resulting in an enhanced net pressure applied across the piezo terminals. The elevated net pressure results in a larger acoustical energy input to the piezo at f_s and therefore larger available electrical power from the piezo. Thus, the minimum piezo volume can be achieved when operating at f_s and as long as R_{Th} is scaled (using AR, see Fig. 2(d)) to match the load impedance, R_L. According to Fig. 2(d), however, R_{Th} at f_s has a finite range, meaning that for large R_L values (>5 kΩ in Fig. 2(d)), impedance matching cannot be achieved at f_s. Therefore, for $R_L > 5$ kΩ, two possible designs exist: (I) operation at f_p with matched piezo-load impedances ($R_L = R_{Th,p}$), and (II) operation at f_s without impedance matching ($R_L \neq R_{Th,s}$). The general equation describing the relationship between the piezo available power, P_a, required power delivered to the load, P_L, the piezo and load impedances R_{Th} and R_L is given by

$$P_L = 4P_a \frac{R_{Th}}{R_L} \left(1 + \frac{R_{Th}}{R_L}\right)^{-2}. \tag{1}$$

Using (1) and known R_L, the two previously described designs can be compared. Two design examples are to follow to demonstrate the process. At f_s, the piezo with an aspect ratio of 1/4 has the highest volumetric efficiency and the largest $R_{Th,s}$ compared to other configurations, making it the best geometry for power delivery to large R_L values. Therefore, only AR of 1/4

for design II needs to be considered for the comparison. Now lets compare the two designs when $R_L = 16\,\text{k}\Omega$ (for moderately high power consumption ICs). A piezo with an aspect ratio of 1 at f_p has $R_{Th,p}$ of 16 kΩ, Fig. 2(d). Therefore, according to (1), $P_L = P_{a,p}$ for this design. The series resonating piezo with AR of 1/4 has $R_{Th,s}$ of 5 kΩ, so $P_L = 0.72 P_{a,s}$, meaning that for this configuration only 72% of the available power is delivered to $R_L = 16\,\text{k}\Omega$ due to the piezo-load impedance mismatch. Therefore, the available power curves in Fig. 2(f) for the two designs are respectively scaled by 1 and 0.72 for arbitrary P_L as shown in Fig. 2(h) for comparison. It can be observed from Fig. 2(h) that for $R_L = 16\,\text{k}\Omega$ operation at f_s (without impedance matching) results in a 4.7x smaller piezo volume compared to operation under maximum power transfer condition at f_p. As another example for ultra-low-power ICs, consider the case where $R_L = 800\,\text{k}\Omega$. For this load, impedance matching and therefore $P_L = P_{a,p}$ can be obtained at f_p by choosing AR of 1/4, Fig. 2(d). Conversely, the series resonating piezo with AR of 1/4 has $R_{Th,s} = 5\,\text{k}\Omega$, resulting in $P_L = 0.025 P_{a,s}$, meaning that for this configuration only 2.5% of the available power is delivered to $R_L = 800\,\text{k}\Omega$. Therefore, the available power curves in Fig. 2(f) for the two designs are respectively scaled by 1 and 0.025 for arbitrary P_L as shown in Fig. 2(i) for comparison. Unlike the previous example, operation at f_s is found to require 2x larger piezo volume to deliver the same amount of power to the load compared to operation at f_p.

In summary, the design approach that results in the minimum implant piezo volume is as follows. For a given R_L and P_L, the aspect ratio of the implant piezo is designed to obtain $R_{Th,s} = R_L$ at f_s. Using Fig. 2(f) and known P_L and AR, the minimum volume of the implant piezo is found and the design is complete. If $R_{Th,s} = R_L$ cannot be achieved at f_s (due to prohibitively small AR), two cases are considered: (I) operation at f_p with matched piezo-load impedances, and (II) operation at f_s without impedance matching. For each case, the required available power by the piezo, P_a, to deliver P_L to the load is found using (1). For P_a calculation, $R_{Th,p} = R_L$ (achieved by proper choice of aspect ratio at f_p) for case (I), and the largest possible $R_{Th,s}$ (smallest possible aspect ratio) is used for case (II). Using calculated P_a and known AR, Fig. 2(f) is used to obtain the piezo volume for case (I) and (II), respectively. Finally, the obtained piezo volumes are compared, and the smaller one is chosen to complete the design.

III. ULTRASOUND BACKSCATTER COMMUNICATION

In a backscatter communication protocol, an interrogation event begins with the interrogator launching a wavelet (denoted as P_{Tx} in Fig. 3) towards the implant. While propagating, P_{Tx} is attenuated and spread out such that only a fraction of its power, P_i, impinges the front face of the implant piezo. The forward path loss (L_f) is used to formally quantify P_i/P_{Tx}. Due to the finite propagation speed of sound in the medium, P_i arrives at the location of the implant after a single time of flight (ToF). At this time, P_i branches into three components: P_E, P_r and P_{leak}: P_E is the harvested electric power available at the electrical terminals of the implant piezo, P_r is the reflected acoustic power
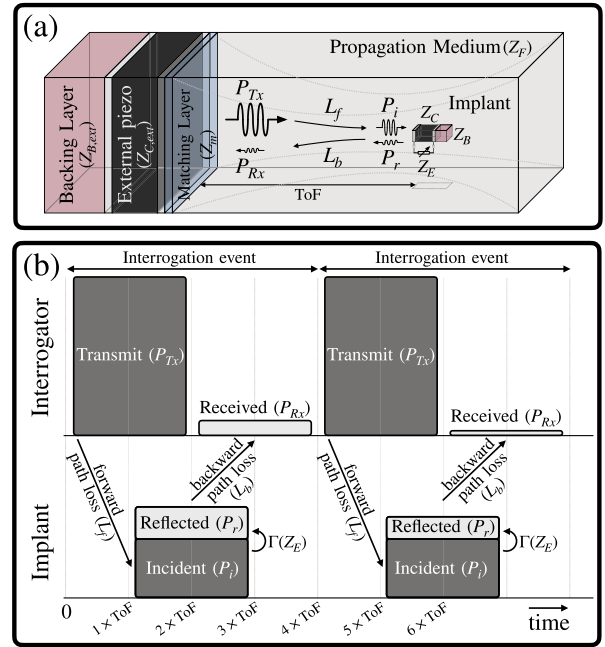

Fig. 3.   (a) Typical backscatter communication channel, and (b) timing diagram of each interrogation event.

and P_{leak} is the power of the wave passing by the implant piezo. The implant IC modulates the piezo acoustic reflection coefficient by adjusting Z_E to encode data for back telemetry, that is $P_r = \Gamma(Z_E)P_i$. It takes another ToF for the wave front of the reflected pressure field P_r to arrive at the location of the external transducer. P_r also experiences attenuation and spreading determined by the backward propagation path loss (L_b). Similar to L_f, L_b is characterized by P_{Rx}/P_r. Finally, the external transducer converts the received pressure field power P_{Rx} into electrical voltage to allow for signal conditioning, demodulation and data postprocessing. Because the same external transducer is used for receiving the backscattered field, the duration of the P_{Tx} wavelet should not exceed the roundtrip travel time ($2\times$ ToF) as shown in the protocol timing diagram in Fig. 3(b).

The complete analysis and end-to-end simulation of the backscatter communication channel described above is challenging mainly for its transient multi-domain electro-acoustical nature. Modeling acoustical systems with equivalent electrical elements is a well-established method for simplifying the analysis [1], [17]–[19]. In this section, we characterize the round-trip channel path loss using a FEM solver. The results obtained from this FEM study are then incorporated into an equivalent circuit model in the next section to simulate the channel response. The roundtrip path loss of the backscatter channel shown in Fig. 3 is given by

$$L_T = \frac{P_{Rx}}{P_{Tx}} = L_f \cdot \Gamma(Z_E) \cdot L_b. \qquad (2)$$

In (2), $\Gamma(Z_E)$ is the backscatter modulating component which will be thoroughly dealt with in the following sections. L_f and L_b are the forward and backward path losses which are 0 dB for a lossless channel. The backscatter channel shown in Fig. 3, has
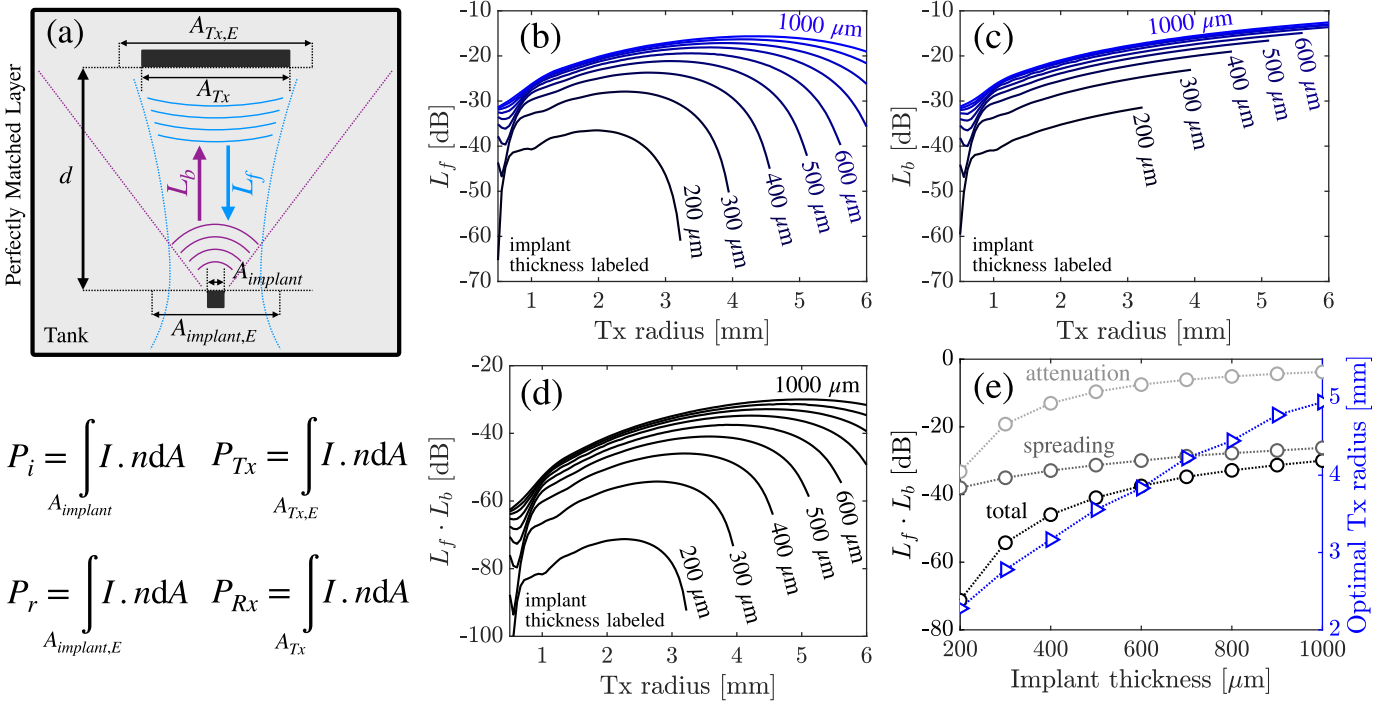
Fig. 4. FEM simulation of channel path loss. (a) Simulation setup. Simulated (b) forward, (c) backward, and (d) round-trip path loss for various implant thicknesses (with aspect ratio of 1) and TX radii. (e) Optimal TX radius and relative contribution of spreading and attenuation components of the path loss.

two contributing loss mechanisms in each direction; attenuation and spreading:

$$L_f = L_{f,a} \cdot L_{f,s} \tag{3}$$

$$L_b = L_{b,a} \cdot L_{b,s}. \tag{4}$$

In (3) and (4), $L_{f,a} \sim L_{b,a} = e^{-2\alpha}$ is the attenuation due to thermal loss of vibrating particles in a viscous propagation medium, where $\alpha = a \cdot f^b$ is the attenuation constant for which a and b are found empirically for the medium of interest, *e.g.* $a = 2.2$ dB/cm.MHz, and $b = 0.8$ for muscle tissue [20]. The spreading loss $L_{f,s}$ is due to the suboptimal radiation pattern of the transmitted field P_{Tx} and the small aperture of the implant piezo. Ideally, all of the transmitted power P_{Tx} is focused on the aperture of the implant piezo and $L_{f,s}$ is 0 dB. But, $L_{f,s}$ degrades when the implant piezo becomes small relative to the dimensions of the foci. Similarly, because the radiation pattern of the backscattered field P_r is approximately spherical, and the aperture of the external transducer is finite, only a fraction of the backscattered power is received by the external transducer resulting in backscattered spreading loss $L_{b,s}$. To quantify the channel path loss, we used a parametric FEM simulation using COMSOL Multiphysics. For the implant piezo with thicknesses ranging from 200 μm to 1000 μm, we simultaneously solved for the optimal aperture of the external transducer and its associated optimal link path loss for a sample depth of 20 mm.

A frequency-domain 2D axisymmetric simulation with a setup shown in Fig. 4(a) was used for this study. For quantifying $L_f (= P_i/P_{Tx})$, P_{Tx} was simulated by assigning a reference pressure boundary condition to the aperture of the external transducer (A_{Tx}). The frequency of the operation was set to the resonant frequency of the implant piezo for each configuration, Fig. 2(b). P_{Tx} and P_i were calculated by integrating the simulated pressure intensity over the cross-sectional area of the external transducer and the implant $A_{Tx,E}$ and $A_{implant}$, respectively, as shown in Fig. 4(a). Here, $A_{Tx,E}$ extends beyond the actual aperture of the external transducer by 100% to account for the entire transmitted power including the side lobes. For each implant piezo thickness, the radius of the external transducer was changed from 0.5 mm to 6 mm and the forward path loss L_f was calculated, shown in Fig. 4(b). It can be observed that for each implant piezo size there exists an optimal transducer radius that results in the minimum forward path loss. A similar parametric simulation was performed to characterize $L_b (= P_{Rx}/P_r)$. That is, a pressure boundary condition was assigned to $A_{implant}$, and P_r and P_{Rx} were calculated by integrating the simulated pressure intensity over $A_{implant,E}$ and A_{Tx}, respectively. The integration cross-sectional area for computing P_r is extended beyond the actual aperture of the implant, $A_{implant}$, by 100% to account for the entire reflected wave power from the implant. Simulated L_b for each implant piezo size and for various apertures of the external transducer are shown in Fig. 4(c). Using simulated L_f and L_b, the roundtrip path loss $L_f \cdot L_b$ was calculated, Fig. 4(d). Comparing Fig. 4(b) and (d), it can be observed that the backward path loss contribution to the roundtrip path loss has moved the optimal radius of the external transducer to slightly larger values. Finally, the roundtrip path loss for a given implant piezo size is shown in Fig. 4(e). The relative contribution of the spreading and attenuation components of the path loss is also shown in Fig. 4(e). Across all implant piezo thicknesses (and consequently operating frequencies) the spreading component
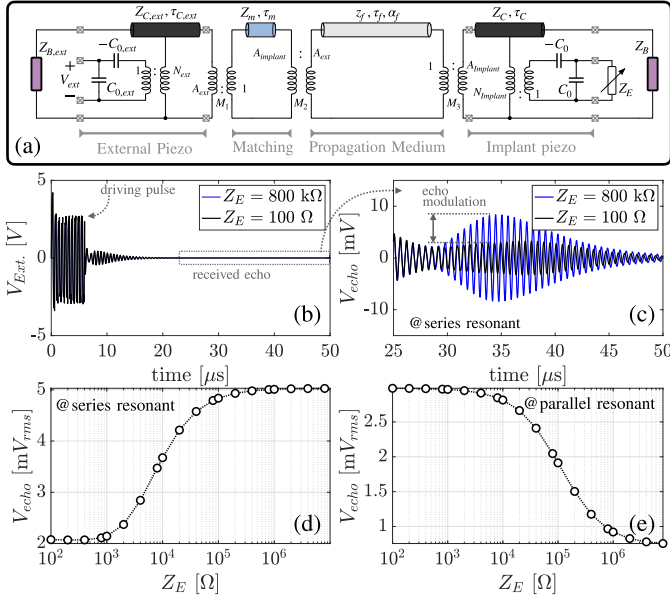
Fig. 5. (a) End-to-end equivalent circuit model of channel. Simulated (b) transient response of channel (c) received echo signal. Received echo vs. Z_E at (d) the series resonant and (e) parallel resonant frequencies.

of the path loss is between 5 to 23 dB larger than the attenuation component. We use the FEM simulated results shown in Fig. 4(e) in the next section to incorporate the effect of path loss in the equivalent circuit model of the channel.

IV. CHANNEL EQUIVALENT CIRCUIT MODEL

In this section, we use an equivalent circuit model, shown in Fig. 5(a), to simulate the backscatter response of the channel in a common CAD tool. As discussed in Section II, low AR piezos resonating in the longitudinal expander (LE) mode provide higher volumetric efficiency for the implants. Due to their high ARs, the piezo elements of the external transducers are usually excited at the thickness extensional (TE) mode to create a directional field towards the target implant [21]. Both LE and TE modes can be represented by the same equivalent circuit model as long as the right material constants are used. Here, we use the Redwood [22] equivalent circuit model for the two piezo elements of the channel, because unlike the Mason [23] or KLM [24], the Redwood model is SPICE friendly. In particular, KLM has a frequency dependent transformer turn ratio that cannot be easily simulated in SPICE. Similarly, Mason requires impedances with unconventional nonlinear frequency dependence that is challenging to implement in common simulation tools. Other derivations of the original Redwood model, such as Leach [25], can equivalently be used in the following analysis as well.

The LE and TE piezoelectric constitutive equations can be collapsed into a set of linear equations as follows [21]

$$\begin{bmatrix} F_1 \\ F_2 \\ V_3 \end{bmatrix} = \mathbf{P} \begin{bmatrix} v_1 \\ v_2 \\ I_3 \end{bmatrix} = \begin{bmatrix} m & n & p \\ n & m & p \\ p & p & r \end{bmatrix} \begin{bmatrix} v_1 \\ v_2 \\ I_3 \end{bmatrix} \quad (5)$$

TABLE I
LIST OF PIEZOELECTRIC TYPICAL PARAMETERS

Parameter	Unit	Value	Description
ρ	kg.m^{-3}	7500	Piezo density
ϵ_{33}^T	nF.m^{-1}	30	Dielectric constant, free
ϵ_{33}^S	nF.m^{-1}	13	Dielectric constant, clamped
s_{33}^E	pm^2.N^{-1}	20.7	Short-circuit elastic compliance
s_{33}^D	pm^2.N^{-1}	9	Open-circuit elastic compliance
e_{33}	C.m^{-2}	23.3	Piezo coupling constant
c_{33}^E	GPa	117	Short-circuit elastic stiffness
g_{33}	V.m.N^{-1}	0.02	Piezo voltage constant
k_{33}	–	0.75	Longitudinal coupling factor
k_t	–	0.5	Thickness coupling factor
W_{imp}	mm	0.4	Implant piezo width
T_{imp}	mm	0.8	Implant piezo thickness
$C_0 = W_{imp}^2 \epsilon_{33}^T (1 - k_{33}^2)/T_{imp}$	pF	2.6	Implant piezo capacitance
$v_{imp} = (\rho s_{33}^D)^{-1/2}$	m.s^{-1}	3851	Implant piezo wave velocity
$\tau_C = T_{imp}/v_{imp}$	ns	208	Implant piezo electrical length
$N_{imp} = g_{33}\epsilon_{33}^T W_{imp}^2/s_{33}^E T_{imp}$	–	0.0057	Implant Redwood turn ratio
$Z_C = \rho v_{imp} W_{imp}^2$	Pa.s.m	4.62	Implant radiation impedance
W_{ext}	mm	0.78	Ext. piezo width
T_{ext}	mm	1.17	Ext. piezo thickness
$C_{0,ext} = W_{ext}^2 \epsilon_{33}^S/T_{ext}$	pF	688	Ext. piezo capacitance
$v_{ext} = ((c_{33}^E + e_{33}^2/\epsilon_{33}^S)/\rho)^{-1/2}$	m.s^{-1}	4600	Ext. piezo wave velocity
$\tau_{C,ext} = T_{ext}/v_{ext}$	ns	254	Ext. piezo electrical length
$N_{ext} = e_{33}W_{ext}^2/T_{ext}$	–	1.23	Ext. Redwood turn ratio
$Z_{C,ext} = \rho v_{ext} W_{ext}^2$	Pa.s.m	2130	Ext. piezo radiation impedance
ρ_f	kg.m^{-3}	1000	Tissue density
v_f	m.s^{-1}	1500	Tissue wave velocity
d	mm	20	Implant-interrogator distance
$Z_{0,f} = \rho_f v_f$	MRayl	1.5	Tissue specific acoustic impedance
$z_f = Z_{0,f}/W_{imp}^2$	TPa.s.m^{-3}	9.37	Tissue characteristic impedance
$\tau_f = d/v_f$	μs	13.3	Time of flight
α_f	dB/m	825	Tissue attenuation constant @d

$$\begin{bmatrix} F_1 \\ F_2 \\ V_3 \end{bmatrix} = \begin{bmatrix} \frac{Z_C}{j\tan(\beta l)} & \frac{Z_C}{j\sin(\beta l)} & \frac{N}{j\omega C_0} \\ \frac{Z_C}{j\sin(\beta l)} & \frac{Z_C}{j\tan(\beta l)} & \frac{N}{j\omega C_0} \\ \frac{N}{j\omega C_0} & \frac{N}{j\omega C_0} & \frac{1}{j\omega C_0} \end{bmatrix} \begin{bmatrix} v_1 \\ v_2 \\ I_3 \end{bmatrix} \quad (6)$$

relating the electrical and the two acoustical ports of a bulk piezo, resonating primarily along its major dimension. In (5) and (6), F and v are respectively force and wave particle velocity at the two acoustical ports of the piezo, while V and I are the voltage and current at its electrical port. The description of the other parameters used in (6) for the external and implant piezo elements in Fig. 5(a) and their typical values used in this study are listed in Table I. The Redwood model directly implements (6). The acoustical ports 1 and 2 are expressed in terms of force (F) and particle velocity (v), and therefore characteristic impedance of the transmission line (Z_C and $Z_{C,ext}$) in the model is the radiation acoustic impedance of the piezo, e.g. $Z_{C,ext} = Z_0 A_{ext}$ where Z_0 is the specific acoustic impedance of the piezo material, and A_{ext} is its cross-section area. The electrical length of the transmission line in the model (τ_C and $\tau_{C,ext}$) is simply set by the physical thickness of the piezo divided by the wave propagation speed in the piezo (see Table I). All the parameters of the Redwood circuit model (C_0, Z_C, τ and N) can be calculated once the piezo material, geometry and type of resonance mode are known. The second acoustical port of each piezo element in Fig. 5(a) is terminated by the radiation acoustic impedance of
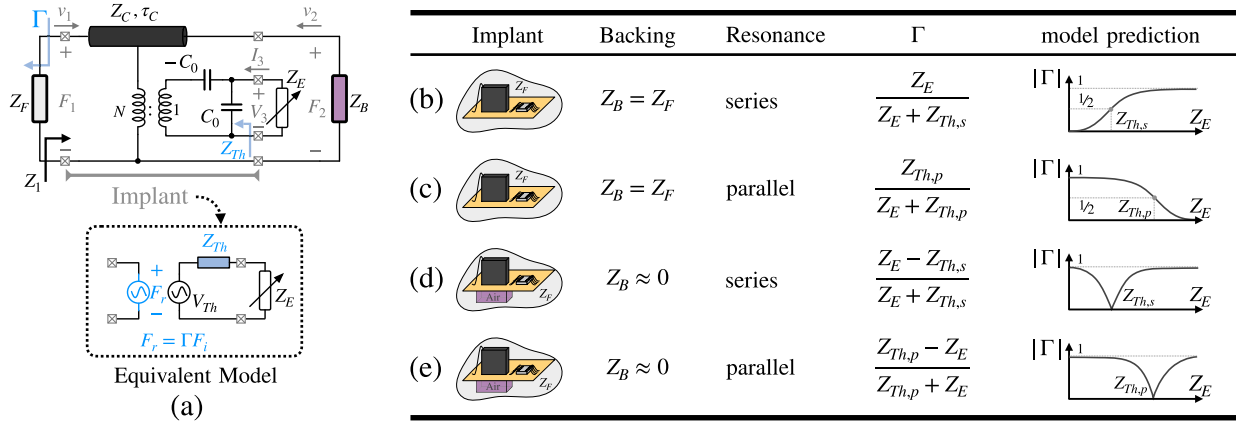
Fig. 6. Proposed piezo electro-acoustical model (a) coupling the Thevenin equivalent circuit model of the piezo to its acoustic reflection coefficient. Expressions for reflection coefficient at parallel and series resonant frequencies for two common backing boundary conditions are listed in (b)-(e).

the backing layer (Z_B and $Z_{B,ext}$). Two transformers M_1 and M_3 are used at the front face of the piezo elements (acoustical port 1) to properly scale F and v by the cross-section area of each piezo (A) and change variables to respectively pressure $p = F/A$ and volume velocity $u = vA$.

A quarter-wavelength matching layer is used at the front (emitting) acoustical terminal of the external transducer to acoustically match the impedance of the external transducer $Z_{C,ext}$ to that of tissue z_f. The characteristic impedance of the matching layer is the geometric mean of the impedances seen to the left and right of the matching layer. A composite of multiple matching layers can also be used to improve the impedance matching bandwidth or in cases where a single matching layer is not feasible (due to unavailability of a material for the required Z_m) [21]. The propagating medium is modeled by a transmission line with the characteristic impedance of z_f and electrical length of τ_f.

In Fig. 5(a), transformer M_2 is used to model a perfect lossless focusing of the beam on the implant aperture. The total FEM simulated roundtrip path loss for an implant piezo with a thickness of $800~\mu m$ is -33 dB at the distance of 20 mm with roughly equal forward and backward loss contributions of -18 and -15 dB, respectively. To account for this path loss, the transmission line modeling the propagation medium is assumed to be lossy with a mean attenuation constant of $\alpha_f = 825$ dB/m. We used *Cadence Virtuoso* to simulate the response of the channel. In this simulation, the external transducer was first driven by 10 cycles of a square wave, and then is immediately short circuited to discharge any residual charge across its terminals. Then, the interrogator is switched to the receive mode to capture the backscattered voltage. A sample transient received backscattered voltage for Z_E of 100 Ω and 800 kΩ is shown in Fig. 5(c) when the operation frequency is tuned to the series resonant frequency of the implant piezo. The implant has no backing layer in this setup. The associated rms voltage of the received echoes for various Z_E values at the series and parallel resonant frequencies of the implant piezo are shown in Figs. 5(d) and (e). It can be observed that the received backscattered signal is a monotonic but nonlinear function of Z_E. Moreover, it behaves differently at the series (increasing

function of Z_E) and parallel resonant frequencies (decreasing function of Z_E).

The end-to-end equivalent circuit model of the channel described above is useful not only for the transient analyses but also for noise analyses and evaluating the response of the channel when a custom active backscatter modulator is used [13]. This circuit, however, lacks simplicity and therefore is not as helpful in the *design* and *synthesis* of novel backscatter modulators. In the next section, we present simple analytically derived expressions for $\Gamma(Z_E)$ that provide insight into critical design aspects of the backscatter modulator.

V. SIMPLIFIED IMPLANT PIEZO MODEL

The Redwood equivalent circuit model of the implant piezo is redrawn in Fig. 6(a)(top). Finding a closed-form relationship between the reflection coefficient evaluated at the front acoustical terminal of the piezo Γ and Z_E is of interest.

[26] formulated the relationship between Z_E and Γ for a resonant piezo and numerically solved for $\Gamma(Z_E)$. We recently expanded the analysis in [26] and analytically derived a closed-form expression for Γ in terms of Z_E [13] for a high-Q piezo operating at its series resonant frequency. Low-Q piezo materials, however, provide a higher fractional bandwidth but have a complex impedance at resonance and therefore the expression derived in [13] needs to be revisited. Similar to the series resonant frequency, characterization of Γ at the parallel resonant frequency of the piezo is also of interest as described in Section II. Air is sometimes used as a backing layer of the implant piezo [27] to reduce mechanical losses and enhance the electro-acoustical efficiency of the implant piezo in exchange for a more complex implant assembly and larger implant volume. Therefore, here we provide closed-form expressions for $\Gamma(Z_E)$ to include: 1) Γ's dependence on Z_E at both the series and parallel resonant frequencies 2) the effect of low-Q mechanically damped piezo, and 3) the effect of air-backing.

By definition, the series and parallel resonant frequencies of a piezo are found for an acoustically unloaded piezo, *i.e.* $Z_F = Z_B = 0$, at which the electrical impedance of the piezo is purely resistive. Therefore, at these two frequencies, the complex
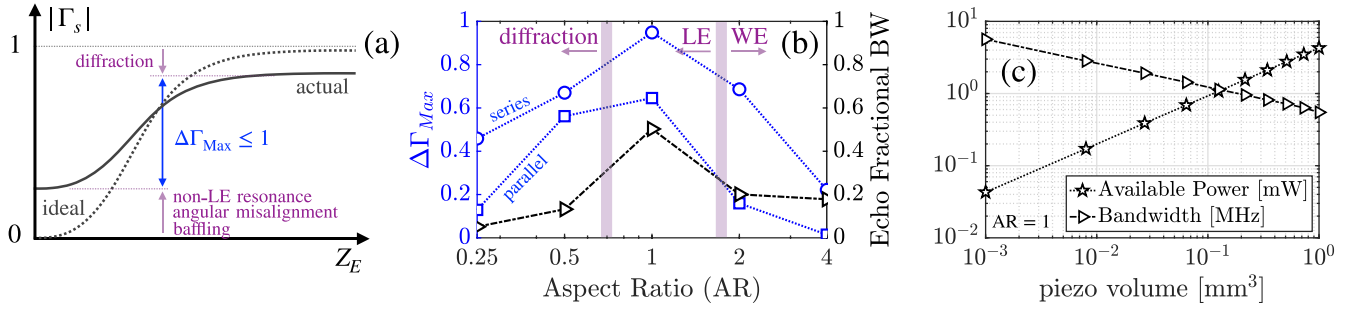
Fig. 7. (a) Non-idealities that degrade $\Delta\Gamma_{\text{Max}}$. FEM simulation results show (b) decreasing the piezo AR initially enhances $\Delta\Gamma_{\text{Max}}$ as the piezo resonance mode changes from width expander (WE) to longitudinal expander (LE), but for AR < 1, $\Delta\Gamma_{\text{Max}}$ starts dropping due to diffraction. The simulated fractional bandwidth of the piezo follows a similar pattern. (c) Simulated available power and backscatter bandwidth for a piezo with an AR of unity.

equivalent electro-acoustical circuit models of the piezo (Mason [23], KLM [24] and Redwood [22]) can be reduced to the piezo Thevenin Equivalent circuit model, using an open-circuit AC voltage source and the piezo internal impedance at the respective resonant frequency. Such a Thevenin equivalent circuit model is very helpful and intuitive due to its simplicity but fails to address the existing coupling between the electrical and acoustical ports of the piezo and ultimately the relationship between Z_E and Γ. Illustrated in Fig. 6(a)(bottom) is the proposed equivalent circuit model of the piezo that fills the electro-acoustical coupling gap of the Thevenin Equivalent circuit model. The proposed model includes a force source and replaces the internal resistance of the piezo with a complex impedance. The force source explicitly generates the reflected acoustic wave (echo) flowing through Z_F, i.e. propagating towards the interrogator. F_i is the force generated by the incident pressure field at the acoustic terminal of the piezo, and Γ is the Z_E-dependent reflection coefficient. Similar to electromagnetic waves, the acoustic reflection coefficient at port 1 of the implant piezo shown in Fig. 6(a)(top) is given by

$$\Gamma = \frac{Z_1 - Z_F}{Z_1 + Z_F}, \tag{7}$$

where Z_1 is the acoustical impedance seen into port 1 when port 2 and 3 are respectively terminated by Z_B and Z_E which is given by

$$Z_1 = \frac{p^2(2n - 2m - Z_B) + (Z_E + r)(m^2 - n^2 + mZ_B)}{(Z_E + r)(m + Z_B) - p^2}. \tag{8}$$

Dummy parameters m, n, p and r in (8) are defined in (5)–(6). By substituting (8) in (7), $\Gamma(Z_E)$ can be found. It is shown in the Appendix that at the series and parallel resonant frequencies, $\Gamma(Z_E)$ can be approximated by

$$\Gamma_s \approx \frac{V_3}{V_{Th}} = \frac{Z_E}{Z_{Th,s} + Z_E}, \tag{9}$$

$$\Gamma_p \approx 1 - \frac{V_3}{V_{Th}} = \frac{Z_{Th,p}}{Z_{Th,p} + Z_E}, \tag{10}$$

when $Z_B = Z_F$, and by

$$\Gamma_{s,air} \approx \frac{Z_E - Z_{Th,s}}{Z_E + Z_{Th,s}}, \tag{11}$$

$$\Gamma_{p,air} \approx \frac{Z_{Th,p} - Z_E}{Z_{Th,p} + Z_E}, \tag{12}$$

for an air-backed implant piezo, i.e. $Z_B = 0$, where Z_{Th} is the electrical impedance of the piezo at the frequency of interest. Interestingly, for an air-backed piezo where there is no flow of energy to the backside acoustic port, the acoustic reflection coefficient at port 1 is equal to the electrical reflection coefficient at port 3, as described by (11) and (12). The proposed electro-acoustical model, shown in Fig. 6(a)(bottom), is well-defined once Z_{Th} at the frequency of operation is known. A summary of the derived expressions under different boundary conditions is listed in Figs. 6(b)–(e).

VI. BACKSCATTER BANDWIDTH

The presented closed-form expressions for the reflection coefficient, (9)–(12), reveal how the amplitude of the echo can be modulated by the piezo termination impedance Z_E for backscatter communication. The modulation range of the echo amplitude is determined by $\Delta\Gamma_{\text{Max}}$, which according to (9)–(12), is ideally equal to 1. $\Delta\Gamma_{\text{Max}}$, however, degrades (and becomes <1) due to second-order effects, mainly caused by the geometry of the implant piezo, that are not well modeled by the piezo constitutive equations used to derive (9)–(12). The type of the piezo resonant mode (LE vs. WE modes), diffraction, angular misalignment, non-ideal backing and baffling are responsible for $\Delta\Gamma_{\text{Max}}$ degradation. These are conceptually outlined in Fig. 7(a) for the case of Γ_s, while FEM simulated $\Delta\Gamma_{\text{Max}}$ at f_s and f_p for various piezo aspect ratios is shown in Fig. 7(b). For AR $\gg$ 1 the piezo resonates more strongly along its width (WE mode) tangential to the direction of the incident wave resulting in reduced $\Delta\Gamma_{\text{Max}}$. For AR < 1, although the piezo resonates in the LE mode, its width becomes considerably smaller than the wavelength of the incident wave so that that wave-piezo interaction is dominated by diffraction rather than reflection. That is, the piezo becomes invisible to the incident wave at AR≪1, significantly reducing its echo modulation strength.
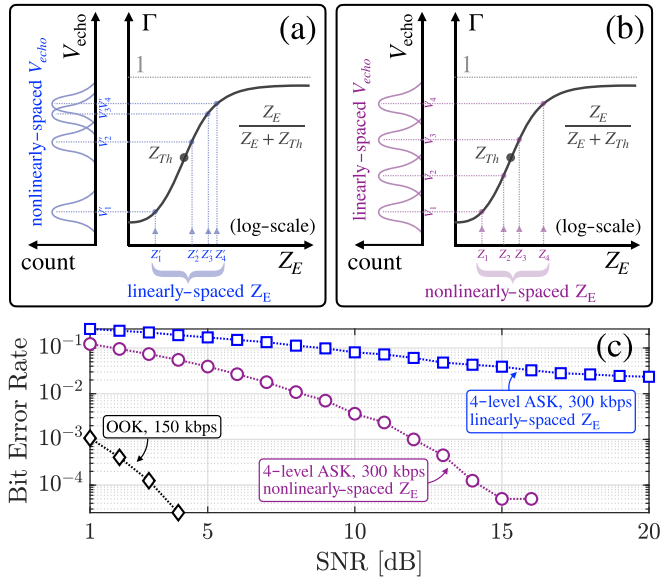
Fig. 8. (a) 4-level ASK backscatter modulation with non-equidistant echo levels due to a suboptimal selection of linearly-spaced modulating Z'_E. (b) optimal 4-level ASK backscatter modulation with equidistant echo levels with nonlinearly-spaced modulating Z_E. (c) Numerically simulated bit error rates for (a), (b) and OOK; 1.5 MHz carrier frequency is used.
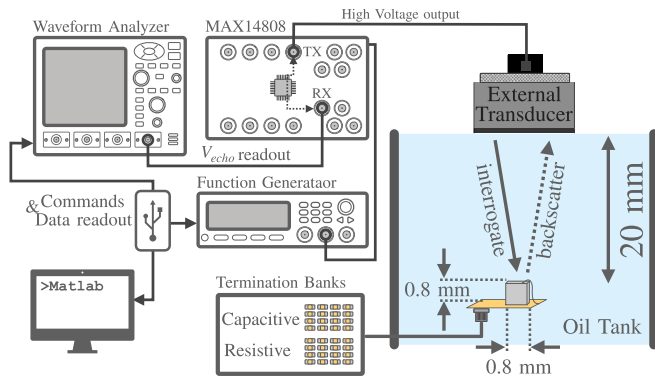

Fig. 9. Experimental setup.

The simulated echo fractional bandwidth of the piezo is also reported in Fig. 7(b). The settling time of the echo when switching Z_E from open- to short-circuit was used to estimate the fractional bandwidth in Fig. 7(b). For AR $\ll$ 1 and AR $\gg$ 1, the piezo uniquely resonates in a distinct resonance mode, respectively LE and WE, resulting in a high quality-factor resonator. At AR$\sim$1, the piezo is in transition from one mode to the other with a reduced quality factor and thus increased fractional bandwidth. Therefore, AR of $\sim$1 is found to be optimal for backscatter communication.

Using the echo fractional bandwidth and the carrier center frequency (Figs. 2(b) and (c)), the available backscatter bandwidth per unit volume of the implant piezo can be calculated as shown in Fig. 7(c). For a given AR (=1 in Fig. 7(c)), increasing the piezo volume (or equivalently thickness) decreases the resonant frequency and ultimately the available backscatter bandwidth. The opposite trends of available power and backscatter bandwidth per unit volume of the implant piezo shown in Fig. 7(c)
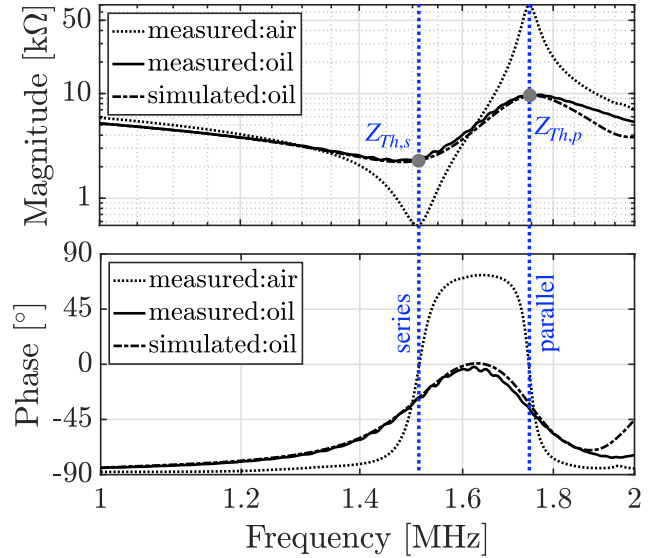

Fig. 10. Measured and simulated piezo impedance.

clearly demonstrate an inherent tradeoff in the geometrical design space of the implant piezo. Thus, for high-speed applications, spectrally efficient backscatter modulation schemes are needed to decouple data rate and available power from the geometry of the implant. For instance, compared to OOK, an m-level amplitude shift keying (ASK) modulation increases the backscatter data rate by a factor of $\log_2(m)$. The selection of termination impedances required to implement an m-level ASK backscatter modulation, however, is not as straightforward as that of OOK and should be made with care as demonstrated in Fig. 8. The echo levels have distributions around their nominal values, due to the noise of the carrier. To reduce the transmission bit error rate (BER), the overlaps between these distributions should be minimized by having equidistant nominal echo levels. The optimal choice of Z_E for equidistant echo levels, shown in Fig. 8(b), can be directly calculated using $Z_E(\Gamma)$ (obtained from (9)–(12)). A comparison of the BER for the two cases in Figs. 8(a) and (b) and OOK is shown in Fig. 8(c) as a function of the carrier signal-to-noise ratio. It can be observed that linearly-spaced modulating Z'_E for the 4-level ASK modulation has an impractically high BER at all SNRs, but non-linearly spaced modulating Z_E can achieve a BER as small as that of OOK at SNR>15 dB while achieving a data rate twice as large.

VII. Measurement and Model Verification

A. Setup

In this section, we use FEM simulation and experimental results to verify the expressions presented in Section V. Here, we only focus on non-air-backed implant piezo model, (9) and (10), as air-backing requires a sealed back-side cavity which complicates implant assembly and potentially degrades the longevity of the implant. The experimental setup is shown Fig. 9. A piezoceramic cube (APC851, 0.51 mm^3) mounted on a flexible board ($\sim$ 0.1 mm thick) was suspended at a distance of 20 mm
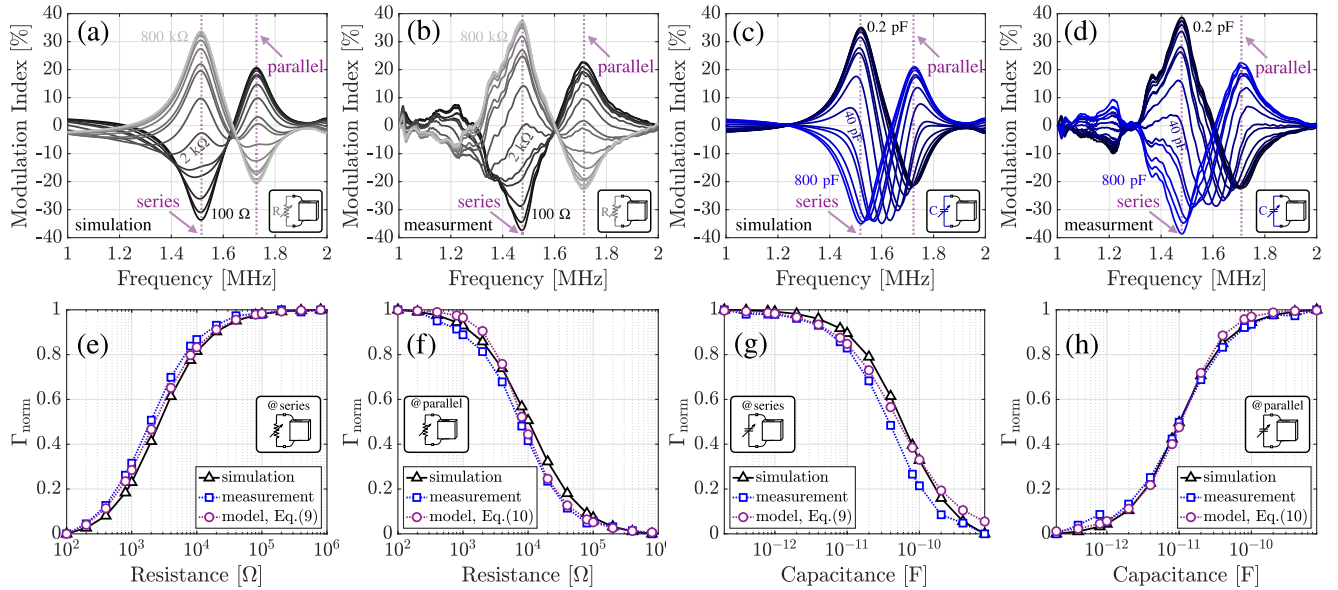
Fig. 11.   (a) Simulated and (b) measured frequency response of the modulation index of the piezo for resistive. (c) simulated and (d) measured frequency response of the modulation index of the piezo for capacitive terminations. Comparison of simulated, measured and predicted Γ_{norm} at (e) f_s and (f) f_p for resistive loads. Comparison of simulated, measured and predicted Γ_{norm} at (g) f_s and (h) f_p for capacitive loads.

away from a $0.25''$ diameter single-element external transducer (Olympus V323-SU) in oil (with attenuation constants $a \sim 0.1$ dB/cm.MHz and $b \sim 1.8$). The external transducer was driven by an ultrasound pulser (Maxim, MAX14808). Each interrogation ultrasound pulse contained 10 ultrasound cycles at a frequency precisely set by a function generator (Keysight 33522B). A waveform analyzer (Keysight CX3300A) was used to record the amplitude of the backscattered waveform received by the external transducer. A custom made capacitive/resistive bank was used to change the termination impedance of the piezo. A PC was used for measurement automation and data collection. An FEM model of the setup shown in Fig. 9 was also generated in COMSOL Multiphysics and used to perform FEM simulations.

B. Results

In order to verify (9) and (10), the impedance of the test piezo was first measured, shown in Fig. 10, using a precision LCR meter (Keysight E4980A). The series and parallel resonant frequencies of the piezo were measured to be 1.5 MHz and 1.745 MHz, respectively. It can be observed in Fig. 10 that submerging the piezo in a viscous fluid, *e.g.* oil, mechanically dampens the piezo and decreases its quality factor so that at f_s and f_p the piezo impedance is no longer purely resistive in oil for this originally low-Q piezo material. The impedance of the piezo is $Z_{Th,s} = 2.31 \; [\mathrm{k}\Omega] \angle - 32°$ and $Z_{Th,p} = 9.78 \; [\mathrm{k}\Omega] \angle - 36°$ at respectively f_s and f_p. The FEM simulated piezo impedance in oil is also shown in Fig. 10 which is in good agreement with the measurement.

Next, the frequency response of the modulation index (MI) of the piezo was measured, for which the frequency of the interrogation pulse was changed from 1 to 2 MHz (in steps of 5 kHz) and the received echo voltage, V_{echo}, was measured. The MI

was calculated for different values of termination impedances (ranging from 100 Ω to 800 kΩ, and 0.2 pF to 800 pF), using the measured V_{echo} and

$$\mathrm{MI} = \frac{V_{echo}(Z_E) - V_{mid}}{V_{mid}}, \tag{13}$$

$$V_{mid} = \frac{1}{2} \left(\max(V_{echo}) - \min(V_{echo}) \right). \tag{14}$$

The simulated and measured frequency response of the MI of the test piezo are shown in Figs. 11(a)-(d). The absolute value of MI has a global and local maxima respectively at f_s and f_p, suggesting that operation at the series resonant frequency of the piezo provides a larger (relative to the midline) backscattered signal. Also, according to Figs. 11(a) and (b), there exists an operation frequency midway between f_s and f_p (~ 1.6 MHz) at which no backscatter modulation is observed for any resistive load. No such frequency is found for capacitive loads, Fig. 11(c) and (d). Moreover, the MI has opposite trends at f_s and f_p with respect to the piezo termination impedance, meaning that at f_s, increasing the termination impedance increases the MI, but at f_p increasing the termination impedance decreases the MI. These trends are shown in Figs. 11(e)-(h) for resistive and capacitive loads. The normalized reflection coefficient

$$\Gamma_{\mathrm{norm}} = \frac{V_{echo}(Z_E) - \min(V_{echo}(Z_E))}{\max(V_{echo}(Z_E)) - \min(V_{echo}(Z_E))}, \tag{15}$$

is plotted in Figs. 11(e)-(h) in order to subtract the measurement environment nonidealities such as non-flat frequency response of the external transducer, frequency dependence path loss and the reflection from the mounting stage of the test piezo. The reflection coefficient predicted by (9) and (10) (using measured $Z_{Th,s}$ and $Z_{Th,p}$ from Fig. 10) is also plotted in Figs. 11(e)-(h).

A good agreement between the simulated, measured and predicted reflection coefficients across a wide range of conditions in Fig. 11 validate the simplifying assumptions made in the derivation of (9) and (10).

VIII. Summary

In this work, we discussed different aspects of a backscatter communication channel with the emphasis on the design and simulation of the implant piezo. First, using the volumetric efficiency as a figure of merit, we presented a design guideline for the aspect ratio and thickness of the implant piezo that minimizes the overall implant volume as far as power harvesting is concerned. We further demonstrated that for maximum backscatter bandwidth and modulation depth the unity aspect ratio is optimal. An end-to-end SPICE friendly equivalent circuit model of the backscatter channel was presented as a tool to simulate the channel response, while incorporating both the attenuation and spreading path loss components of the channel. The channel equivalent circuit model was then used to simulate $\Gamma(Z_E)$, a critical design parameter for backscatter uplink modulation. Last, to gain further insight into $\Gamma(Z_E)$, we presented simple closed form expressions for $\Gamma(Z_E)$ which link Γ to the commonly used Thevenin equivalent circuit model of the implant piezo under various boundary conditions. The experimentally validated closed-form expressions for $\Gamma(Z_E)$ are insightful for the design of ultrasound backscatter modulating circuits.

Appendix

Using (5), (6) and the acoustical boundary conditions ($F_1 = -Z_F v_1$ and $F_2 = -Z_B v_2$) in Fig. 6(a)(top), the impedance seen into the electrical port of the piezo (port 3) is found as follows

$$Z_3 = r - \frac{p^2(Z_B + Z_F + 2(m - n))}{Z_B Z_F + m(Z_B + Z_F) + m^2 - n^2}. \quad (16)$$

Piezo series resonant frequency is a frequency at which the electrical impedance of an acoustically unloaded piezo ($Z_B = Z_F = 0$) has no imaginary component. Therefore, (16) at f_s results in

$$r(m^2 - n^2) = 2p^2(m - n). \quad (17)$$

Here, we use Z_3 instead of the previously used Z_{Th} to make indices compatible with the port numbers used in Fig. 6. Now, let's derive Γ_s for the piezo with $Z_B = Z_F \neq 0$ at f_s. By substituting (8) in (7), and using (16)–(17), Γ_s can be found

$$\Gamma_s = \frac{1}{Z_E + Z_3} \cdot \frac{Z_E(m^2 - n^2 - Z_F^2) - r Z_F^2}{m^2 - n^2 + 2mZ_F + Z_F^2}. \quad (18)$$

Given at f_s, $m^2 - n^2 \gg Z_F^2 + 2mZ_F$ for typical tissue and piezo material constants, (18) can be approximated by

$$\Gamma_s \approx \frac{Z_E}{Z_E + Z_3}, \quad (19)$$

when $Z_B = Z_F \neq 0$. The same procedure can be used to derive $\Gamma_{s,air}$ for an air-backed piezo $Z_B = 0$ operating at f_s. That is,

for an air-backed piezo, (16) becomes

$$Z_{3,air} = r - \frac{p^2(Z_F + 2(m - n))}{mZ_F + m^2 - n^2}$$

$$= Z_F \frac{mr - p^2}{mZ_F + m^2 - n^2}, \quad (20)$$

where the second equality is resulted using (17). By substituting (8) in (7), and using (17) and (20), $\Gamma_{s,air}$ can be found

$$\Gamma_{s,air} = \frac{Z_E - Z_F \frac{mr - p^2}{m^2 - n^2 - mZ_F}}{Z_E + Z_F \frac{mr - p^2}{m^2 - n^2 + mZ_F}} \approx \frac{Z_E - Z_3}{Z_E + Z_3}. \quad (21)$$

At the parallel resonant frequency, $\beta l \to \pi$ and it can be shown that in (5) and (6) $m \to \infty$, $(m - n) \to \infty$, $(m + n) \to 0$ and $(1 - n/m) \to 2$. Using these approximations, when $Z_B = Z_F \neq 0$ at f_p, (16) and (8) can be simplified to

$$Z_3 = r - \frac{2p^2(Z_F + m - n)}{Z_F^2 + 2mZ_F + m^2 - n^2} \approx \frac{-2p^2}{Z_F}, \quad (22)$$

$$Z_1 = Z_F - \frac{4p^2}{Z_E + r} \approx Z_F\left(1 + \frac{2Z_3}{Z_E}\right). \quad (23)$$

Γ_p can therefore be found by substituting (23) in (7), that is

$$\Gamma_p \approx \frac{Z_3}{Z_E + Z_3}. \quad (24)$$

In a similar fashion, $\Gamma_{p,air}$ for an air-backed piezo $Z_B = 0$ operating at f_p can be derived. In this case, Z_3 and Z_1 are given by

$$Z_3 = r - \frac{p^2(Z_F + 2(m - n))}{mZ_F + m^2 - n^2} \approx \frac{-4p^2}{Z_F}, \quad (25)$$

$$Z_1 = -\frac{4p^2}{Z_E + r} \approx \frac{Z_F Z_3}{Z_E}, \quad (26)$$

and using (7), $\Gamma_{p,air}$ is found as

$$\Gamma_{p,air} \approx \frac{Z_3 - Z_E}{Z_3 + Z_E}. \quad (27)$$

Acknowledgment

References

[1] D. Seo et al., "Wireless recording in the peripheral nervous system with ultrasonic neural dust," Neuron, vol. 91, no. 3, pp. 529–539, 2016.
[2] M. M. Ghanbari et al., "17.5 a 0.8 mm^3 ultrasonic implantable wireless neural recording system with linear AM backscattering," in Proc. IEEE Int. Solid-State Circuits Conf., 2019, pp. 284–286.
[3] D. K. Piech et al., "A wireless millimetre-scale implantable neural stimulator with ultrasonically powered bidirectional communication," Nature Biomed. Eng., vol. 4, no. 2, pp. 207–222, 2020.
[4] K. Laursen, A. Rashidi, S. Hosseini, T. Mondal, B. Corbett, and F. Moradi, "Ultrasonically powered compact implantable dust for optogenetics," IEEE Trans. Biomed. Circuits Syst., vol. 14, no. 3, pp. 583–594, Jun. 2020.
[5] M. J. Weber, Y. Yoshihara, A. Sawaby, J. Charthad, T. C. Chang, and A. Arbabian, "A miniaturized single-transducer implantable pressure sensor with time-multiplexed ultrasonic data and power links," IEEE J. Solid-State Circuits, vol. 53, no. 4, pp. 1089–1101, Apr. 2018.

[6] B. A. Ozilgen and M. M. Maharbiz, "Ultrasonic thermal dust: A method to monitor deep tissue temperature profiles," in *Proc. IEEE 39th Annu. Int. Conf. Eng. Med. Biol. Soc.*, 2017, pp. 865–868.

[7] C. Shi, T. Costa, J. Elloian, Y. Zhang, and K. Shepard, "A 0.065-mm^3 monolithically-integrated ultrasonic wireless sensing mote for real-time physiological temperature monitoring," *IEEE Trans. Biomed. Circuits Syst.*, vol. 14, no. 3, pp. 412–424, Jun. 2020.

[8] S. Sonmezoglu and M. M. Maharbiz, "34.4 a 4.5 mm^3 deep-tissue ultrasonic implantable luminescence oxygen sensor," in *Proc. IEEE Int. Solid-State Circuits Conf.*, 2020, pp. 454–456.

[9] M. Meng, P. Graybill, R. L. Ramos, A. Javan-Khoshkholgh, A. Farajidavar, and M. Kiani, "An ultrasonically powered wireless system for in vivo gastric slow-wave recording," in *Proc. 41st Annu. Int. Conf. IEEE Eng. Med. Biol. Soc.*, 2019, pp. 7064–7067.

[10] M. M. Maharbiz *et al.*, "Implants using ultrasonic backscatter for sensing electrical impedance of tissue," U.S. Patent App. 16/313,860, May 23 2019.

[11] H. Kawanabe, T. Katane, H. Saotome, O. Saito, and K. Kobayashi, "Power and information transmission to implanted medical device using ultrasonic," *Japanese J. Appl. Phys.*, vol. 40, no. 5S, pp. 3865–3866, 2001.

[12] F. Mazzilli *et al.*, "In-vitro platform to study ultrasound as source for wireless energy transfer and communication for implanted medical devices," in *Proc. IEEE Annu. Int. Conf. Eng. Med. Biol.*, 2010, pp. 3751–3754.

[13] M. M. Ghanbari *et al.*, "A sub-mm^3 ultrasonic free-floating implant for multi-mote neural recording," *IEEE J. Solid-State Circuits*, vol. 54, no. 11, pp. 3017–3030, Nov. 2019.

[14] D. Berlincourt, "Piezoelectric crystals and ceramics," *Ultrasonic Transducer Materials*. Boston, MA, USA: Springer, 1971, pp. 63–124.

[15] "Marketing clearance of diagnostic ultrasound systems and transducers," Jun. 27, 2019. [Online]. Available: https://www.fda.gov/media/71100/download, Accessed: Sep. 6, 2020.

[16] H. Azhari, *Basics of Biomedical Ultrasound for Engineers*. Hoboken, NJ, USA: Wiley, 2010.

[17] L. E. Kinsler, A. R. Frey, A. B. Coppens, and J. V. Sanders, "Fundamentals of acoustics," *Fundam. Acoust.*, 4th Ed., pp. 560. ISBN 0-471-84789-5. Wiley-VCH, Dec. 1999, Art. no. 560.

[18] H. Basaeri, D. B. Christensen, and S. Roundy, "A review of acoustic power transfer for bio-medical implants," *Smart Mater. Structures*, vol. 25, no. 12, 2016, Art. no. 123001.

[19] S. H. Song, A. Kim, and B. Ziaie, "Omnidirectional ultrasonic powering for millimeter-scale implantable devices," *IEEE Trans. Biomed. Eng.*, vol. 62, no. 11, pp. 2717–2723, Nov. 2015.

[20] D. Nassiri, D. Nicholas, and C. Hill, "Attenuation of ultrasound in skeletal muscle," *Ultrasonics*, vol. 17, no. 5, pp. 230–232, 1979.

[21] G. S. Kino, *Acoustic Waves: Devices, Imaging, and Analog Signal Processing*, vol. 107. Englewood Cliffs, NJ, USA: Prentice-Hall, 1987.

[22] M. Redwood, "Transient performance of a piezoelectric transducer," *J. Acoust. Soc. Amer.*, vol. 33, no. 4, pp. 527–536, 1961.

[23] D. A. Berlincourt, D. R. Curran, and H. Jaffe, "Piezoelectric and piezomagnetic materials and their function in transducers," *Phys. Acoust.: Principles Methods*, vol. 1, no. Part A, p. 247, 1964.

[24] R. Krimholtz, D. A. Leedom, and G. L. Matthaei, "New equivalent circuits for elementary piezoelectric transducers," *Electron. Lett.*, vol. 6, no. 13, pp. 398–399, 1970.

[25] W. M. Leach, "Controlled-source analogous circuits and spice models for piezoelectric transducers," *IEEE Trans. Ultrason., Ferroelect. Freq. Control*, vol. 41, no. 1, pp. 60–66, Jan. 1994.

[26] S. Ozeri and D. Shmilovitz, "Simultaneous backward data transmission and power harvesting in an ultrasonic transcutaneous energy transfer link employing acoustically dependent electric impedance modulation," *Ultrasonics*, vol. 54, no. 7, pp. 1929–1937, 2014.

[27] T. C. Chang, M. J. Weber, J. Charthad, S. Baltsavias, and A. Arbabian, "End-to-end design of efficient ultrasonic power links for scaling towards submillimeter implantable receivers," *IEEE Trans. Biomed. Circuits Syst.*, vol. 12, no. 5, pp. 1100–1111, Oct. 2018.

Mohammad Meraj Ghanbari (Student Member, IEEE) received the M.Eng. and M.Phil. degrees in electrical engineering, from the University of Melbourne, Victoria, Australia, in 2013 and 2016, respectively. He is currently working toward the Ph.D. degree in electrical engineering and computer sciences with the University of California, Berkeley, CA, USA. His research interests include analog and mixed-signal integrated circuits, energy harvesting, sensor interfaces, biosensing and neural recording. Mr. Ghanbari was the recipient of the MIRS/MIFRS scholarships in 2013, Kenneth Myers Memorial Scholarship in 2014, the Department of EECS Fellowship in 2016, and the ADI Outstanding Student Designer Award in 2019.

Rikky Muller (Senior Member, IEEE) received the B.S. and M.S. degrees from Massachusetts Institute of Technology, Cambridge, MA, USA, and the Ph.D. degree from the University of California at Berkeley, Berkeley, CA, USA, all in electrical engineering and computer sciences (EECS). She previously held positions as an IC Designer with Analog Devices, Wilmington, MA, USA, and as a McKenzie Fellow and a Lecturer of EE with the University of Melbourne, Melbourne, VIC, Australia. She was also the Co-Founder of Cortera Neurotechnologies, Inc., Berkeley, a medical device company founded in 2013 and acquired in 2019, where she held positions as CEO and CTO. She is currently the S. Shankar Sastry Assistant Professor in emerging technologies with the EECS Department, University of California at Berkeley. She is also the Co-Director of the Berkeley Wireless Research Center, a Core Member of the Center for Neural Engineering and Prostheses, University of California at Berkeley, and an Investigator with the Chan-Zuckerberg Biohub, San Francisco, CA, USA. Her expertise is in the research and commercialization of implantable medical devices and in developing integrated circuits (ICs) and systems for neurological applications. Dr. Muller is a member of the technical program committee for IEEE ISSCC, and has previously served on the committees of IEEE CICC and BioCAS. She has also served as a Guest Editor for the IEEE JOURNAL OF SOLID-STATE CIRCUITS. She was the recipient of numerous fellowships and awards, including the National Academy of Engineering Gilbreth Lectureship, the Chan-Zuckerberg Biohub Investigatorship, the Keysight Early Career Professorship, the Hellman Fellowship, the Bakar Fellowship, the NSF CAREER Award, and the McKnight Technological Innovations In Neuroscience Award. She was named one of MIT Technology Reviews top 35 global innovators under the age of 35 (TR35), and one of MedTech Boston's top 40 healthcare innovators under 40.